Visualizing strongly-correlated electrons with a novel scanning tunneling microscope

Battisti, I.

2

The experimental technique: spectroscopic-imaging scanning tunneling microscopy

2.1 Scanning tunneling microscopy

The working principle of scanning tunneling microscopy (STM) is based on quantum tunneling. To achieve tunneling, a sharp metallic tip is brought close to the flat surface of a conducting sample (typically a few angstroms), as illustrated in Fig. 2.1a. When a bias voltage is applied between tip and sample, electrons can tunnel through the vacuum gap between the two, just as they tunnel through a potential barrier in textbook, one-dimensional quantum tunneling [21]. This creates a measurable tunneling current, typically of the orders of pico- to nanoamperes, that decays exponentially with the distance between tip and sample. The tip is then scanned over the surface using a feedback loop that keeps the tunneling current constant by adjusting the tip-sample distance. By recording the vertical position of the tip at every location, a topographic image of the surface is created.

In Fig. 2.1b, we show an example of such an STM image (from now on called *topograph*) measured on the top BiO layer of a $Bi_2Sr_2CaCu_2O_{8+\delta}$ (BSCCO) sample. Atomic resolution is achieved, with the Bi atoms visible on the surface. The additional long-wavelength vertical corrugation is typical of the material and commonly called supermodulation. Importantly, the contrast in STM topographs is given by a mixture of geometrical height and electronic structure, whose contributions cannot generally be separated from each other.

The main motivation of Binnig and Roher, who invented STM and won a Nobel prize for it, was, however, not to construct a scanning probe technique, but to have an instrument able to perform tunneling spectroscopy locally on an area less than 100 Å in diameter [22]. Tunneling spectroscopy is a very powerful tool, and the combination of topographic information with spatially-resolved spectroscopy is indeed what made STM so important for understanding solid-state physics, and in particular quantum materials.

The process of incorporating spectroscopy in STM quickly developed from the first pioneering experiments on semiconductors [23] and metals [24, 25] to the study of BCS superconductors [26] and unconventional high-T_c superconductors. It is on the latter materials that the technique manifested its full potential, because they have an intrinsically inhomogeneous electronic structure at the nanoscale [15, 16]. Overall, performing spectroscopy with STM greatly outperformed the 100 Å-resolution goal of Binnig and Roher, since the technique can easily distinguish the effect of single impurity atoms on the density of states with picometer resolution [27, 28].

In the rest of this chapter, we motivate why the combination of STM with tunneling spectroscopy is ideally suited to study quantum matter. We start by showing that STM gives a local view into the density of states by deriving the expression for the tunneling current and the tunneling spectra (Sec. 2.1.1). We then introduce the tech-

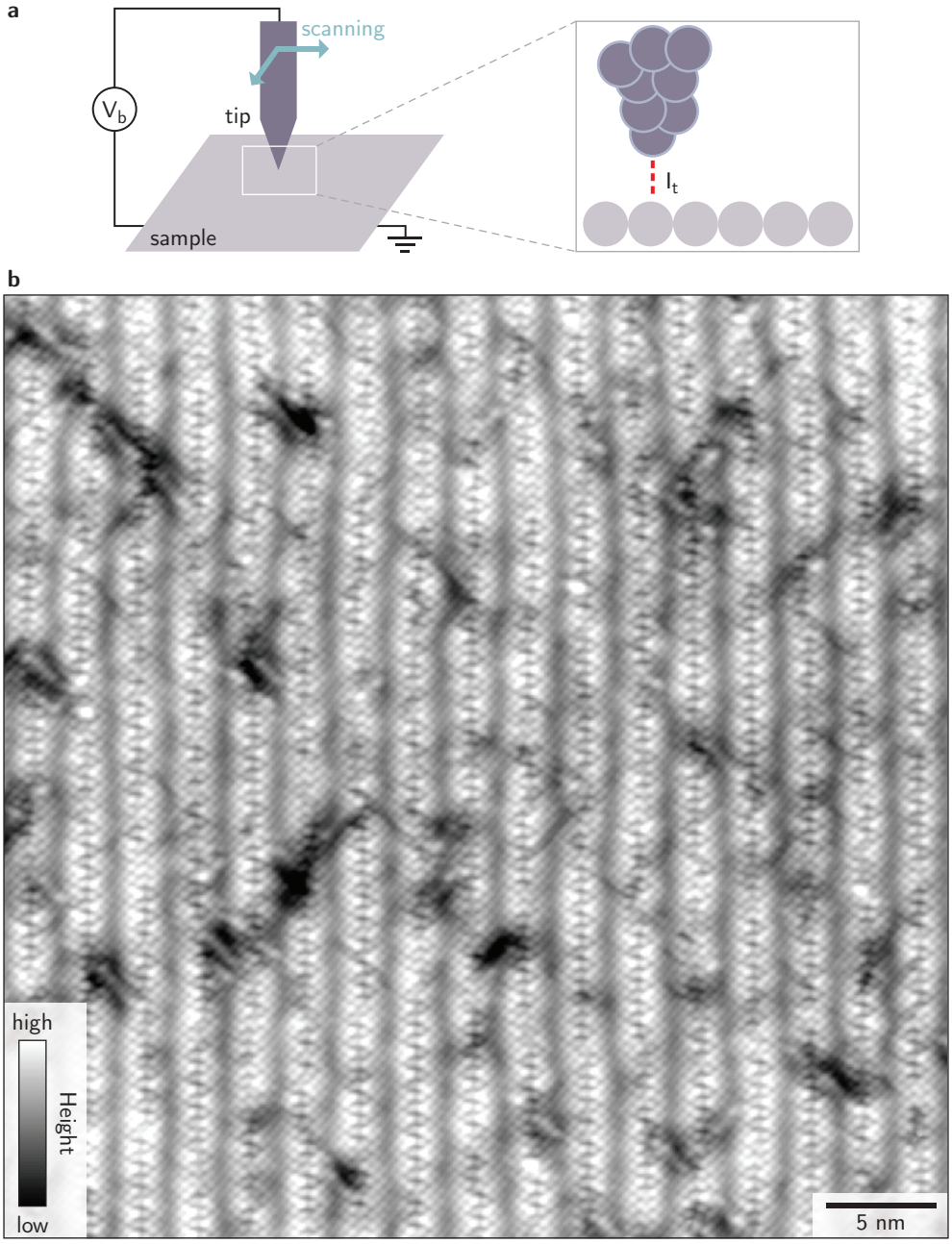

Figure 2.1: **a**, Cartoon picture of the working principle of an STM. **b**, Topograph measured on an underdoped $Bi_2Sr_2CaCu_2O_{8+\delta}$ sample ($T_c = 40\,K$). The field of view is $43 \times 43\,nm^2$ and the setup conditions are (V_b=160 mV, I_t=80 pA). Atoms and the extra corrugation known as supermodulation are resolved. Some defects of unknown origin are also visible on the surface.

nique of spectroscopic-imaging STM (Sec. 2.2), that yields powerful 3-dimensional datasets. We discuss several possibilities to analyze these datasets in order to obtain deep insights into the physics of the materials, both in real and in momentum space (Sec. 2.3). Finally, we introduce a tip-induced artifact that we will encounter in chapters 4 and 5 of this thesis (Sec. 2.4), and we conclude with a comment on energy resolution in STM (Sec. 2.5).

2.1.1 STM as a probe of the local density of states

Here, we give a brief derivation of the tunneling current between tip and sample, illustrating how it is related to the *local* density of states (LDOS) of the sample [29, 30].

In Fig. 2.2, the density of states of tip and sample, $g_{\mathrm{t}}(\epsilon)$ and $g_{\mathrm{s}}(\epsilon)$, respectively, are sketched next to each other. The tip is a good metal, and therefore its density of states (DOS) can be considered flat in the proximity of the Fermi level, while the sample has, in general, a more complicated DOS. If tip and sample are electrically connected, the two chemical potentials μ_{t} and μ_{s} are aligned at the same energy. Applying a positive bias voltage V_{b} to the sample causes its chemical potential μ_{s} to shift downwards by eV_{b} with respect to μ_{t}. Now, electrons can tunnel from the occupied states of the tip to the empty states of the sample within the energy window eV_{b}. At finite temperatures, the occupation probability for the electronic states is given by the Fermi-Dirac distribution

$$f(\epsilon, T) = \frac{1}{1 + \exp[(\epsilon - \mu)/(k_{\mathrm{B}}T)]}, \tag{2.1}$$

where μ is the chemical potential and k_{B} the Boltzmann constant. The number of occupied states on the tip at energy ϵ is therefore given by $g_{\mathrm{t}}(\epsilon) \cdot f(\epsilon, T)$, while the number of available states on the sample is $g_{\mathrm{s}}(\epsilon) \cdot [1 - f(\epsilon, T)]$. From now on, for simplicity, we set the chemical potential of the sample at zero energy, $\mu_{\mathrm{s}} = 0$. This is indeed the convention that is used in real STM measurements.

The tunneling current from tip to sample can be calculated as the integral over all energies of the number of filled states on the tip times the number of empty states on the sample. There is also a small contribution of electrons tunneling from the sample to the tip. The total tunneling current can obtained by summing this two opposite currents, and it is expressed as:

$$I(V_{\mathrm{b}}, h) = -2e\frac{2\pi}{\hbar}\int_{-\infty}^{+\infty} |M(h)|^2 \left[f(\epsilon) - f(\epsilon - eV_{\mathrm{b}})\right] g_{\mathrm{s}}(\epsilon)\, g_{\mathrm{t}}(\epsilon - eV_{\mathrm{b}})\, \mathrm{d}\epsilon. \tag{2.2}$$

Here, the factor 2 takes the two possible spin states into account, the factor $2\pi/\hbar$ is derived from perturbation theory, and $|M(h)|^2$ represents the tunneling matrix

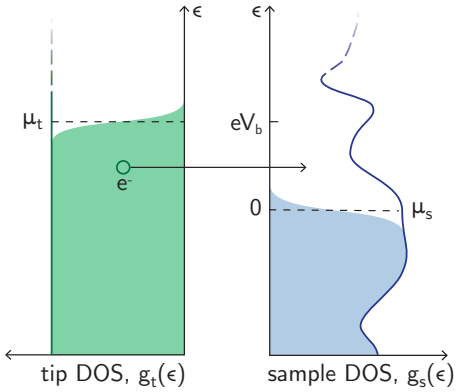

Figure 2.2: Schematic representation of the tunneling process between tip and sample density of states.

elements, which contain the exponential dependence of the tunneling current on the tip-sample distance h. The broadening of the Fermi-Dirac distribution is quantified by $k_\mathrm{B}T$. At liquid helium temperature, where all measurements reported in this thesis are performed, $k_\mathrm{B}T = 0.36\,\mathrm{meV}$. This is very sharp compared to typical features in the DOS, and therefore we can approximate the Fermi-Dirac distribution by a step function. This significantly simplifies the tunneling current to

$$I(V_\mathrm{b}, h) = \frac{4\pi e}{\hbar} \int_0^{eV_\mathrm{b}} |M(h)|^2 \, g_\mathrm{s}(\epsilon) \, g_\mathrm{t}(\epsilon - eV_\mathrm{b}) \, \mathrm{d}\epsilon. \tag{2.3}$$

Under the realistic assumptions that the tunneling matrix elements do not depend on energy and that g_t is flat in energy (a condition that is verified before every measurement by obtaining a flat DOS on a featureless gold sample), the expression for the tunneling current can be further simplified:

$$I(V_\mathrm{b}, h) = \frac{4\pi e}{\hbar} |M(h)|^2 \, g_\mathrm{t} \int_0^{eV_\mathrm{b}} g_\mathrm{s}(\epsilon) \, \mathrm{d}\epsilon. \tag{2.4}$$

The tunneling current therefore depends directly on both tip-sample separation h and the integrated sample density of states. Since STM probes the sample locally, it actually measures the *local* density of states, $\mathrm{LDOS}(\mathbf{r}, \epsilon = eV_\mathrm{b})$, defined as the number of electrons per unit volume and energy at a given point in space $\mathbf{r}$ and at a given energy ϵ [29].

Since the tunneling current is proportional to the integrated sample LDOS, its derivative with respect to the bias voltage (the differential conductance) is proportional to

the local density of states of the sample:

$$\frac{\partial I(V_\mathrm{b}, h)}{\partial V_\mathrm{b}} = \frac{4\pi e^2}{\hbar} |M(h)|^2 \, g_\mathrm{t} \, g_\mathrm{s}(eV_\mathrm{b}) \, . \tag{2.5}$$

This is exactly what is measured in a tunneling spectroscopy experiment, and it is commonly called a $\mathrm{d}I/\mathrm{d}V$ tunneling spectrum.

In practice, in order to acquire such a spectrum, the tip is brought in tunneling with setup conditions $(V_\mathrm{s}, I_\mathrm{s})$. This means that a bias voltage V_s is applied, and the feedback adjusts the tip-sample distance until the current reaches I_s. The feedback is then switched off and the bias voltage is swept while recording changes in the current to obtain a current-voltage (IV) curve. For bias voltage $V_\mathrm{b} > 0$ applied to the sample, electrons will tunnel from tip to sample, probing the unoccupied sample states. For $V_\mathrm{b} < 0$, electrons will tunnel from sample to tip, probing the occupied sample states.

Taking the numerical derivative of such acquired IV curves provides the sample LDOS as a function of energy. However, numerical derivatives usually enhance the noise. To overcome this problem, it is standard technique to use a lock-in amplifier to modulate the bias voltage with an amplitude $\mathrm{d}V$ and to directly measure the demodulated value of the current $\mathrm{d}I$. In this way, the differential conductance can be directly measured as a $\mathrm{d}I/\mathrm{d}V$ spectrum, where the energy resolution is given by the amplitude of the lock-in modulation. Typical modulations that are used in the work presented in this thesis range from 2 meV (rhodates, chapter 6) to 50 meV (low doping level iridates, chapter 4).

2.1.2 Tunneling into many-body systems: Green's functions and spectral functions

The density of states, that we used to describe the tunneling current so far, is a well-defined concept only for non-interacting electrons. In this case, the available energies for given states with wave vector $\mathbf{k}$ are defined by the dispersion relation. In correlated electron systems, however, even when $\mathbf{k}$ is well defined, the electron-like quasiparticle can exchange energy with other quasiparticles due to interactions. It is then better to use the formalism of many-body systems and express the relevant quantities through Green's functions and spectral functions. A good, full introduction to these concepts can be found in Ref. [31, 32]; here, we focus on expressing the quantities measured with STM in terms of these concepts.

The spectral function $A(\mathbf{k}, \omega)$ can be seen as a generalized version of the density of states for many-body systems, since it represents the probability of finding a single-particle excitation at a given energy ω and momentum $\mathbf{k}$. The tunneling equation can be fully derived using spectral functions instead of density of states, leading to the same final result that the tunneling current is proportional to the integrated local

density of states [32]. The local density of states can in fact be expressed as the *local* spectral function $A(\mathbf{r},\omega) = \sum_{\mathbf{k}} A(\mathbf{k},\omega;\mathbf{r})$, which is in turn related to the many-body retarded Green's function $G(\mathbf{r},\omega)$ by:

$$\mathrm{LDOS}(\mathbf{r},\omega) = A(\mathbf{r},\omega) = -\frac{1}{\pi}\mathrm{Im}[G(\mathbf{r},\omega)]. \tag{2.6}$$

STM tunneling spectra therefore measure the local (in real-space) spectral function averaged over all momenta [32, 33].

Experimentalists in strongly correlated electron systems are often acquainted with the concept of spectral functions from angle-resolved photoemission spectroscopy (ARPES), which directly measures the spectral function in momentum space. We show how the two techniques compare in section 2.3.1.

2.2 Spectroscopic-imaging STM

We now introduce spectroscopic-imaging STM[1], which is the most powerful technique to measure topographic and spectroscopic information simultaneously. It consists of measuring a $\mathrm{d}I/\mathrm{d}V$ spectrum for every pixel of a simultaneously acquired topograph. The result is a three-dimensional dataset representing the local density of states as function of position and energy, $\mathrm{LDOS}(r_x, r_y, \epsilon)$. Such a dataset is commonly called a *spectroscopic map*. Most of the data presented in this thesis is collected in this form.

A typical spectroscopic map contains 10^4–10^5 $\mathrm{d}I/\mathrm{d}V$ spectra, that are acquired one after the other. The feedback is only active when moving the tip to the new location, and switched off while acquiring the spectra. This makes this type of measurement extremely sensitive to external vibrations. Such a measurement can last from one to several days (it is typically limited by the hold time of the cryostat). SI-STM therefore puts highest demands on the stability of the microscope.

A spectroscopic map is extremely rich in information which can be extracted and analyzed in several different ways. In Fig. 2.3, we show a visual representation of a spectroscopic map, together with examples of data analysis options that are used throughout this thesis. One can look at the data 'vertically' (i.e. along the energy), analyzing the $\mathrm{d}I/\mathrm{d}V$ spectra one by one. For example, it is interesting to observe how they change with location, and how they are influenced by the presence of a dopant atom or an impurity in the crystal. This can be well visualized in *waterfall* plots. Additionally, a properly chosen function can be fitted to every single spectrum to extract locally changing parameters. A well-known example is extracting the width

[1] Note that the terms spectroscopic-imaging STM (SI-STM), Fourier-transform STM (FT-STM) and scanning tunneling spectroscopy (STS) are often used interchangeably. Here, we will use the convention SI-STM.

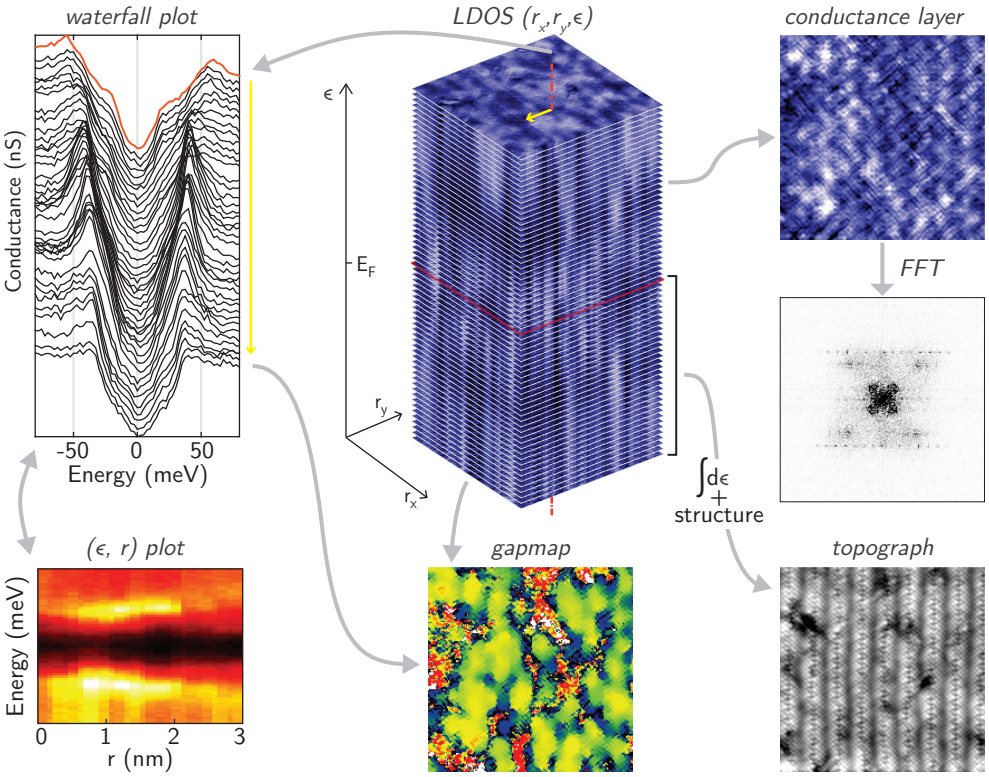

Figure 2.3: SI-STM generates 3-dimensional datasets. Exploring the data along different directions opens many data analysis options. The data shown as example is measured on an underdoped $Bi_2Sr_2CaCu_2O_{8+\delta}$ sample (T_c= 40 K). The field of view is 21×21 nm^2.

of the superconducting gap in unconventional superconductors [16]. This can then be used to build a so-called *gapmap*, where the magnitude of the gap is given as an intensity plot as function of location. Alternatively, one can look at the data 'horizontally' (i.e. along the spatial coordinates), directly analyzing the constant-energy conductance layers. They can reveal spatially organized structures hinting towards charge order or wave-like patterns indicating quasiparticle interference. When the conductance layers show periodicity, their Fourier transform can provide additional quantitative information.

2.3 Probing momentum space: quasiparticle interference

SI-STM is a direct probe for real space properties, but it can also access momentum space information through quasiparticle interference (QPI) imaging. This technique has been initiated by observing standing waves caused by QPI on the surface of Cu(111) [24]. Briefly afterwards, it was realized that quantitative information about the scattering vectors could be obtained by Fourier transforming the images of the standing waves pattern [25]. The technique has since then been extensively used, and it proved to be particularly powerful in the study of unconventional superconductors [18, 34–36], heavy fermions [37, 38] and topological insulators [39–41]. In the present section, we briefly explain the phenomenon of quasiparticle interference using the simple example of a metal, based on Ref. [30]. The concepts that we introduce here will then be applied in chapter 6 to study QPI in the correlated metal Sr_2RhO_4.

In an ideal metal, the quasiparticle eigenstates are Bloch wave functions with the periodicity of the crystal lattice. They are characterized by the momentum $\mathbf{k}$, and their energy must follow the dispersion relation $\epsilon(\mathbf{k})$. The presence of crystal defects or impurities causes elastic scattering of the quasiparticles, that mixes states with different wave vectors $\mathbf{k}_1$, $\mathbf{k}_2$ but same energy $\epsilon(\mathbf{k})$. The result of scattering are standing waves with wave vectors $\mathbf{q}(\epsilon) = \mathbf{k}_1(\epsilon) - \mathbf{k}_2(\epsilon)$. These standing waves and their interference pattern can be directly imaged in the conductance layers of spectroscopic maps measured with SI-STM.

In Fig. 2.4a, we show an example of standing waves on Cu(111) caused by quasiparticles scattering off a single impurity on the surface. By taking the two-dimensional

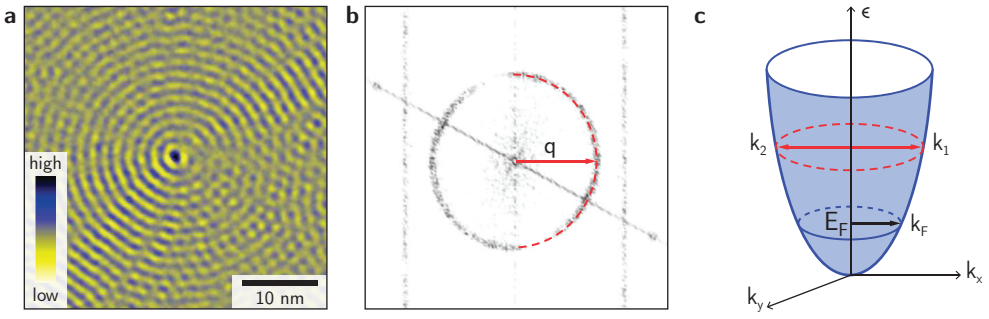

Figure 2.4: **a**, QPI on Cu(111) in real space: conductance layer at 50 meV around a single impurity scattering center. The field of view is 45 nm^2. Adapted from Ref. [42]. **b**, QPI in Fourier space: Fourier transform of panel **a**. Adapted from Ref. [42]. **c**, Cartoon picture representing the band structure of a 2D metal.

Fourier transform of such a conductance layer, an image in momentum space is obtained, as shown in Fig. 2.4b. Here, the magnitudes of the quasiparticle scattering vectors $\mathbf{q}$ are plotted as a function of direction. The pattern seen in the Fourier transformed images is related to the band structure of the material. For a 2D electron gas, the band structure is a paraboloid where the constant energy contours are circles with radius $k(\epsilon)$, as illustrated in Fig. 2.4c. The Fourier transform of the conductance layers will therefore be dominated by circles with radius $q(\epsilon) = 2k(\epsilon)$. The QPI pattern in real and momentum space will evolve with energy, reflecting the increasing diameter of the constant energy contours. By tracking the magnitude of scattering vectors $\mathbf{q}$ as a function of energy, one can measure their dispersion and extract information about the electronic properties of the material.

In general, it is challenging to identify the origin of the scattering vectors $\mathbf{q}$ without previous knowledge of the band structure. In a simplistic picture, the wave vectors $\mathbf{q}$ that dominate the QPI pattern correspond to a large joint DOS (JDOS) of pairs of $\mathbf{k}$ vectors. High JDOS can arise from regions in k-space where the constant energy contours are parallel, as for example in the quasi one-dimensional bands of Sr_2RuO_4 [43]. Alternatively, high JDOS arises from scattering that connects flat regions in the dispersion, where the density of states is significantly larger. In cuprates, this is at the origin of the well-known octet model for QPI in $Bi_2Sr_2CaCu_2O_{8+\delta}$ [18].

2.3.1 Comparing STM and photoemission

The most successful direct probe of momentum space is angle-resolved photoemission spectroscopy (ARPES), which is also a surface sensitive technique. Having seen that STM can also be used as a (indirect) probe for momentum space, it is interesting to compare its results with the ones of ARPES.

ARPES is based on the photoelectric effect. A beam of photons incident on the surface of a material can excite and eventually cause the emission of electrons from the material. By directly measuring the energy and momentum of the emitted electrons, one can reconstruct the band structure. Under a series of approximations (that go under the name of *sudden approximation*), the photocurrent measured by ARPES can be expressed in terms of the single-particle spectral function, $A(\mathbf{k}, \omega)$, as [44]:

$$I_{\mathrm{ARPES}}(\mathbf{k}, \omega) = I_0 \, |M_{f,i}|^2 \, f(\omega) \, A(\mathbf{k}, \omega), \tag{2.7}$$

where $M_{f,i}$ represents the photoemission matrix elements, and $f(\omega)$ is the Fermi-Dirac distribution.

We showed in section 2.1.2 that STM probes the local density of states, which can be expressed as the (real-space) local spectral function averaged over all momenta. The ARPES signal, on the other hand, is proportional to the spectral function in

momentum space, averaged over a real-space area corresponding to the photon beam size [32]:

$$I_{\mathrm{STM}} \propto A(\mathbf{r},\omega) = -\frac{1}{\pi}\,\mathrm{Im}\,[G(\mathbf{r},\omega)], \tag{2.8}$$

$$I_{\mathrm{ARPES}} \propto A(\mathbf{k},\omega) = -\frac{1}{\pi}\,\mathrm{Im}\,[G(\mathbf{k},\omega)]. \tag{2.9}$$

STM and ARPES data cannot be mathematically related to each other simply by a spatial Fourier transform, because their relationship involves terms that are not measured [33].

However, in a simplified JDOS picture for the origin of QPI, STM data can still be compared with ARPES through autocorrelation approaches [45–47]. Here, high JDOS for the scattering vectors $\mathbf{q}$ can be described as [47]:

$$\mathrm{JDOS}(\mathbf{q},\omega) = \int A(\mathbf{k}+\mathbf{q},\omega)A(\mathbf{k},\omega)\,\mathrm{d}^2k. \tag{2.10}$$

This corresponds to the autocorrelation of constant energy ARPES images when photoemission matrix elements are neglected. This approach to compare STM QPI and ARPES data is very simplified, though it is useful to at least qualitatively recognize the origin of the scattering vectors observed in FT-STM images.

We use this autocorrelation approach in chapter 6, to aid the identification of scattering vectors observed on the correlated metal Sr_2RhO_4.

2.4 STM on materials with poor electronic screening

The tunneling current equation obtained in Sec. 2.1.1 assumes as a starting point that the sample is metallic. STM experiments can, however, also be performed on materials that have a small gap around the Fermi level (up to 2-3 eV), such as semiconductors or lightly doped Mott insulators. These materials, differently than metals, are characterized by poor electronic screening, which can affect the interpretation of STM results.

We encounter such a situation in our STM measurements on Sr_2IrO_4 (chapter 4), which leads to some artifacts in the data. Here, we give a brief introduction to this phenomenon, and derive how it affects the tunneling current equation (2.4). Chapter 5 is dedicated to explore this effect in more detail, in order to have a correct interpretation of the experimental data measured on materials with poor elecronic screening.

To understand the effect of poor electronic screening in STM measurements, we consider a standard tip-sample configuration, and assume for simplicity that the bias

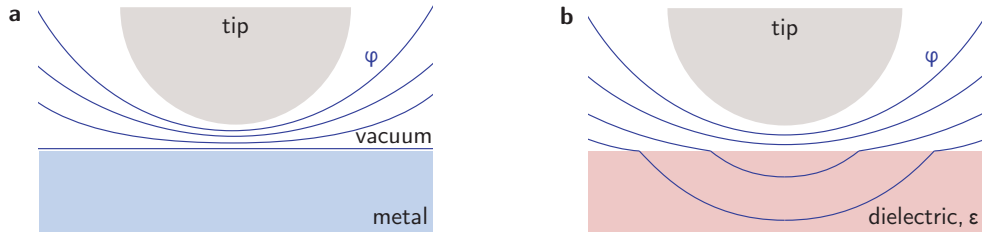

Figure 2.5: Equipotential lines in STM experiments showing different screening of electric fields in different materials. **a**, In standard STM experiments on metals, the electric field generated by the tip is largely screened within the first atomic layer and there is no significant field penetration. **b**, In samples with a gapped density of states at the chemical potential, the electric field can penetrate the sample due to poor electronic screening.

voltage is applied to the tip. When a metallic sample like copper is placed in the electric field generated by the STM tip, the field is almost perfectly screened and the sample has a uniform potential. If the bottom of the sample is grounded, the full sample will be at zero electric potential, and the tunneling equation Eq. (2.4) holds. This scenario changes if the sample is not a metal: the electric field generated by the tip can then partially penetrate the sample surface, causing an additional potential drop inside the sample. This is schematically depicted in Fig. 2.5. Because the potential landscape in the sample changes in a way similar to how bands bend at semiconductor interfaces, this effect is known as *tip-induced band bending* (TIBB) [48–50].

Tip-induced band bending will affect the tunneling equations because the surface of the sample directly below the STM tip will not be at zero potential, but at some finite potential φ_{BB}. The tunneling current in the presence of band bending at $T \sim 0\,\mathrm{K}$ is therefore given by

$$I(V_{\mathrm{b}}, h) = \frac{4\pi e}{\hbar}\,|M(h)|^2 \int_0^{eV_{\mathrm{b}}-\varphi_{\mathrm{BB}}(V_{\mathrm{b}},h)} g_s(\epsilon)\, g_t\big(\epsilon - eV_b + \varphi_{\mathrm{BB}}(V_{\mathrm{b}}, h)\big)\,\mathrm{d}\epsilon, \qquad (2.11)$$

which, in the assumption of constant tip DOS, simplifies to

$$I(V_{\mathrm{b}}, h) = \frac{4\pi e}{\hbar}|M(h)|^2\, g_t \int_0^{eV_{\mathrm{b}}-\varphi_{\mathrm{BB}}(V_{\mathrm{b}},h)} g_s(\epsilon)\,\mathrm{d}\epsilon. \qquad (2.12)$$

It is essential to know the expression for φ_{BB} if one wants to extract quantitative information about the LDOS from tunneling spectroscopy experiments. In the semiconductor community, the phenomenon of TIBB is well known, and methods to compute φ_{BB} in order to get a correct interpretation of the data are available (for example, the Poisson's equation solver developed by Feenstra [51]). In lightly doped Mott insulators, on the other hand, the phenomenon of TIBB is less studied, and the models developed for semiconductors cannot be applied. In chapter 5, we thoroughly discuss

the phenomenon of TIBB for this case, with an application to the lightly doped Mott insulator Sr_2IrO_4.

2.5 Thermal broadening and energy resolution in STM

To obtain the expression for the tunneling current shown in Eq. (2.4), we approximated the Fermi-Dirac distribution by a step function. This is licit only when $T = 0\,\mathrm{K}$, because for any finite temperature the Fermi-Dirac function has a finite spread of a few $k_\mathrm{B}T$ that broadens all features in energy.

Taking this into account, the question arises of how much the thermal broadening will affect the energy resolution of tunneling spectroscopy. The finite temperature expression for $\mathrm{d}I/\mathrm{d}V$ spectra can be obtained by taking the derivative of Eq. (2.2):

$$\frac{\partial I(V_\mathrm{b})}{\partial V_\mathrm{b}} \propto \int_{-\infty}^{+\infty} g_\mathrm{s}(\epsilon)\, \frac{\partial f(\epsilon - eV_\mathrm{b})}{\partial V_\mathrm{b}}\, \mathrm{d}\epsilon \tag{2.13}$$

The derivative of the Fermi-Dirac distribution shows a peak of height $1/(4k_\mathrm{B}T)$ centered at $\epsilon = eV_\mathrm{b}$. A standard measure for the energy resolution is given by the FWHM of this peak [4], that can be easily evaluated being

$$\Delta E = k_\mathrm{B}T \cdot [\ln(3 + 2\sqrt{2}) - \ln(3 - 2\sqrt{2})] = 3.53\, k_\mathrm{B}T\,. \tag{2.14}$$

The energy resolution at 4.2 K is therefore 1.3 meV. We have seen that the resolution of a $\mathrm{d}I/\mathrm{d}V$ spectrum directly measured with a lock-in amplifier is given by the amplitude of the voltage modulation $\mathrm{d}V$. Thermal broadening therefore puts a fundamental lower limit for the smallest value of $\mathrm{d}V$.